PAPER

Check for updates

Bifunctional π-conjugated ligand assisted stable and efficient perovskite solar cell fabrication *via* interfacial stitching†

Feijie Wei,[a] Bo Jiao,[ab] Hua Dong, [ID] *[ab] Jie Xu,[a] Ting Lei,[a] Junjie Zhang,[c] Yue Yu, [ID] [cd] Lin Ma, [ID] [d] Dongdong Wang, [ID] [c] Jinbo Chen,[a] Xun Hou[a] and Zhaoxin Wu [ID] *[ab]

Ligand-assisted interface engineering has been considered as a promising strategy to improve the performance and stability of perovskite solar cells (PSCs) simultaneously. Due to the insulating properties of conventional non-conjugated ligands, trap passivation is always at the expense of the interface/bulk carrier transport of the perovskite film. To overcome this paradox, a functional organic amine salt, 3-phenyl-2-propen-1-amine iodide, (PPEAI), is introduced to modify the interfacial characteristics of perovskite films *via* an "interfacial stitching effect". This typical ligand could effectively contribute to the suppression of surface defects and ion migration. Furthermore, improved charge transport behavior of perovskite films can be achieved due to the conjugation and delocalization characteristics of PPEAI. By employing the optimized PPEAI modified perovskite film, a 21.01% efficiency was obtained from the champion device, with good stability under both ambient conditions and operation conditions without encapsulation.

Introduction

Nowadays, organic–inorganic hybrid perovskites (OIHP) have attracted much attention in the photovoltaic community due to their merits such as high absorption coefficient, high charge carrier mobility, long electron–hole diffusion lengths, and a simple low-temperature solution based fabrication process.[1–3] The reported highest power conversion efficiency (PCE) of OIHP-based photovoltaic cells has surpassed 23%, starting from 3.8% in 2009.[4–9] Nowadays, numerous perovskite materials have been reported as the photoactive layer, and the structural and optical–electrical properties of the perovskite can be regulated by varying the composition and proportion of the cations/anions. Compared with popular photoactive materials, such as MA (methylammonium)- and FA (formamidinium)-based perovskite materials, "triple-cation" perovskites (Cs/MA/FA) offer the possibility of higher power conversion efficiency, moisture content, and thermal stability.[10–18] However, the as-prepared perovskite films always display a large density of defects on the surface as well as in the interior of the perovskite bulk inevitably. The defect-induced non-radiative recombination and ion migration could limit the device performance and photocurrent hysteresis behavior.[19–24] Meanwhile, moisture corrosion still occurs in "triple-cation" perovskites, leading to poor stability. These issues are still barriers to their commercialization potential.

Recently, ligand-induced modification engineering has been demonstrated as a feasible concept to achieve stable and high-performance PSCs. By employing hydrophobic and large-sized organic molecules, such as phenethylamine, benzylamine, aminovaleric acid, and pentafluoropropylamonium,[25–29] mixed 2D–3D systems show superior moisture stability compared with solely 3D perovskite. Moreover, long-chain cations could effectively passivate the trap states of the initial perovskite film, restricting non-radiative recombination as well as preventing ion migration.[13] However, considering the insulating property of long-chain non-conjugated molecules and low carrier mobility of passivated fragments, effective ligand passivation always comes at the price of the charge transport offset in the perovskite bulk. How to break the predicament of simultaneously maximizing performance and stability of the device is the top priority of developing the industry.

In this work, a bifunctional π-conjugated organic amine salt, 3-phenyl-2-propen-1-amine iodide (PPEAI) (shown in Fig. S1†), was employed as the typical interfacial modifier. By utilizing

[a] Key Laboratory for Physical Electronics and Devices of the Ministry of Education, Shaanxi Key Lab of Information Photonic Technique, School of Electronic and Information Engineering, Xi'an Jiaotong University, No. 28, Xianning West Road, Xi'an, 710049, China. E-mail: donghuaxjtu@mail.xjtu.edu.cn; zhaoxinwu@mail.xjtu.edu.cn

[b] Collaborative Innovation Center of Extreme Optics, Shanxi University, Taiyuan 030006, China

[c] Department of Chemistry, School of Science, Xi'an Jiaotong University, Xi'an 710049, China

[d] School of Physics and Optoelectronic Engineering, Xidian University, Xi'an 710071, China

† Electronic supplementary information (ESI) available. See DOI: 10.1039/c9ta03898a

This journal is © The Royal Society of Chemistry 2019

J. Mater. Chem. A, 2019, **7**, 16533–16540 | 16533

this ligand, we demonstrated a dual improvement of both optoelectronic performance and stability of the perovskite solar cells *via* an interfacial engineering process. Benefiting from the "stitching effect" of PPEAI, surface defects of the perovskite film can be healed *via* coordination with I iron. Meanwhile, due to the chain/ring conjugated peculiarity, a denser electron cloud overlapping and delocalization effect can be induced in PPEAI,[30] promoting the charge transport in the perovskite framework.

According to density functional theory (DFT) calculations, both the benzene ring part and alkyl chain part of PPEAI contributed to the HOMO and LUMO, which demonstrated the excellent conductivity of this aniline molecule. Under the optimal treatment by PPEAI, the modified device exhibits a champion efficiency of 21.01%, which showed a significant improvement compared to the control device with a PCE of 17.98%. Moreover, significantly improved stability can be observed from the PPEAI modified devices under both ambient conditions (92% of the original PCE for 1000 h) and operation conditions (85% of the original PCE for 300 h) without encapsulation. This work provides a novel principle for passivation molecular design and will pave a new way for high performance and long-term stable perovskite solar cells.

Results and discussion

Characteristics of films and materials

Fig. 1 shows the typical solvent post-treatment engineering. Here the preparation method of the 3D perovskite film used a conventional one-step anti-solvent process. Specifically, concentration-controlled long-chain ligands in an anti-solvent could achieve effective passivation during the film crystallization process, which induced the formation of a low-dimensional capping layer on the surface and grain boundaries (GBs) of the 3D structure. Fig. 2a–d show the SEM images of the as-prepared and PPEAI modified perovskite films (1 mg mL^{-1}, 2 mg mL^{-1} and 5 mg mL^{-1} PPEAI in chlorobenzene). As for the 1 mg mL^{-1} and 2 mg mL^{-1} of PPEAI, it can be seen that there is no obvious

morphological variation before and after the treatment, and the latter just shows a little more compact morphology and increased polycrystal grains. However, high concentration PPEAI (5 mg mL^{-1}) induced the slight anomalous surface morphology compared to the original perovskite film. From the size distribution (shown in Fig. S2†), small-sized crystal grains (<100 nm) appeared on the perovskite film treated with 5 mg mL^{-1} PPEAI compared with the other three films (as-prepared, 1 mg mL^{-1} PPEAI, 2 mg mL^{-1} PPEAI).

We also investigated the component characteristics with XRD measurements (shown in Fig. 2e). It can be seen that all films showed similar diffraction patterns, attributed to the typical 3D perovskite peaks.[29,31,32] Compared to the control film, PPEAI treated samples exhibit a stronger intensity diffraction peak, reflecting the improved film crystallinity. New XRD diffraction peaks below 10 degrees were observed in the perovskite film treated with 5 mg mL^{-1} PPEAI. Compared with those of the reference 2D perovskite films (PPEA$_2$PbI$_4$) (shown in Fig. S3†), the newly formed peak positions in the perovskite with 5 mg mL^{-1} PPEAI agree well with the typical 2D phase. Here we noticed that the new characteristic diffraction peaks were not observed in the low-concentration PPEAI films (1 mg mL^{-1} PPEAI and 2 mg mL^{-1} PPEAI), possibly due to the 2D perovskite fragments being too thin to be detected. Moreover, we noticed that the position of the (110) 3D perovskite peak shifted toward lower angles when the concentration of PPEAI increased (shown in Fig. S4†), and the shift of the diffraction peak reflected the crystal unit expansion in the perovskite framework due to substitution of the bromide ions by iodide ions into the perovskite lattice.[32]

Here the full width at half maximum (FWHM) and the position of the (110) peak pattern were further estimated in the enlarged region. As the concentration of PPEAI increased, gradually narrowed FWHM and increased intensity were observed, which can be attributed to the progressive trap passivation at the grain boundaries and the surface of the films. While the high concentration of PPEAI led to a wider FWHM, we speculated that the excessive low-dimensional fragments
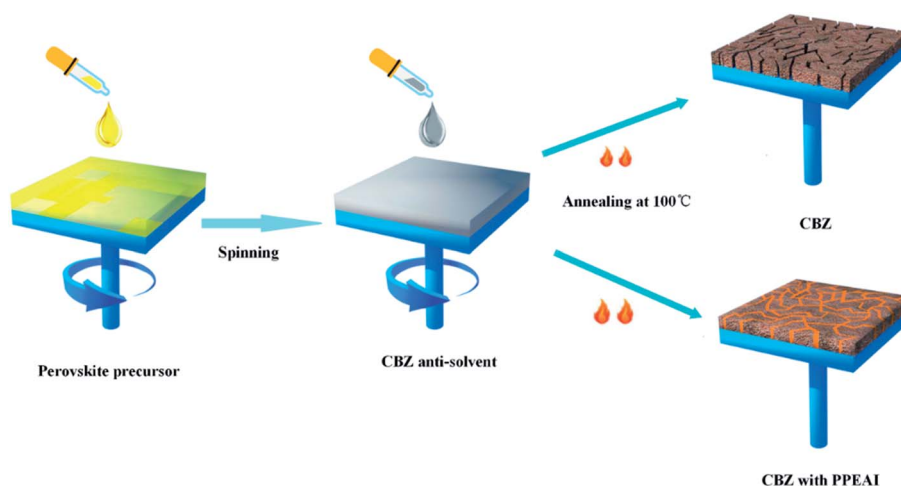

Fig. 1 Above: Schematic illustration of the spin-coating process for fabricating perovskite films with an anti-solvent process; below: the PPEAI induced surface/GB passivation process.
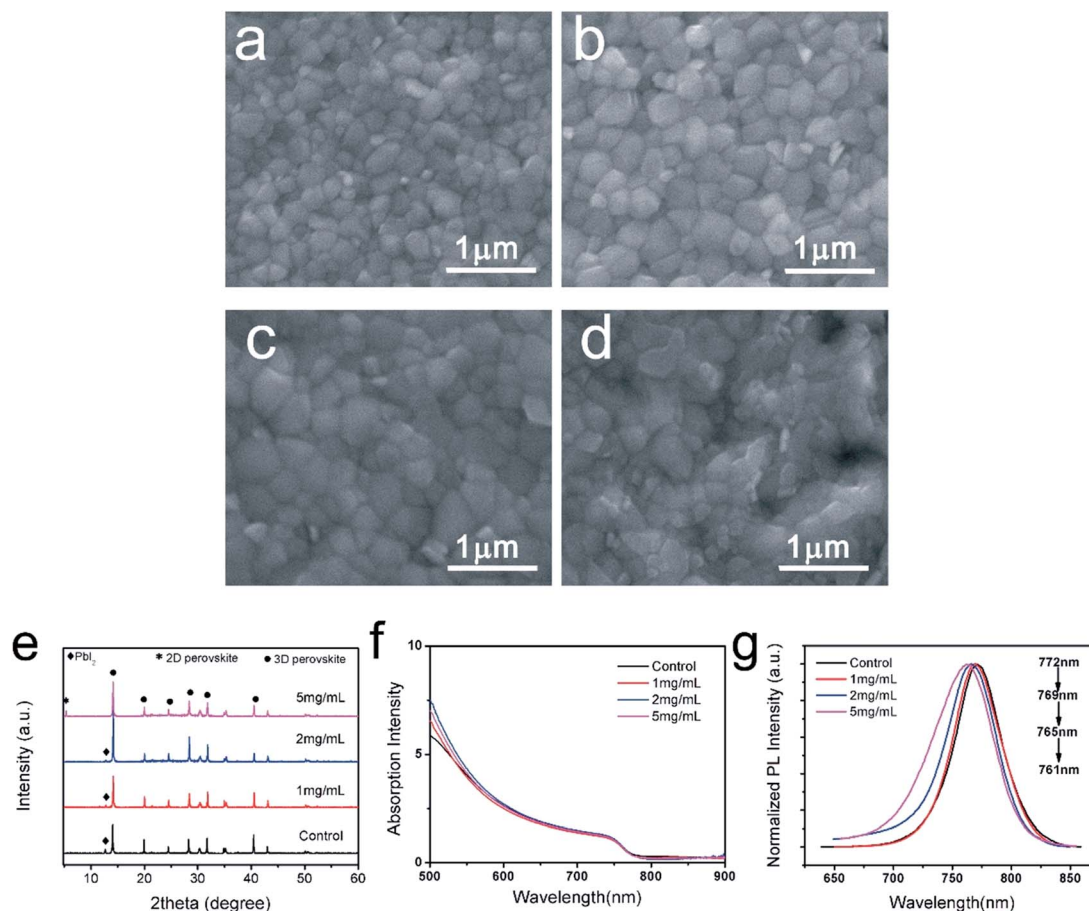
Fig. 2 (a–d) Top-view SEM images of the control and PPEAI modified films (0 mg mL^{-1}, 1 mg mL^{-1}, 2 mg mL^{-1}, and 5 mg mL^{-1}); (e) XRD data, (f) absorption spectra and (g) PL spectra of the control and PPEAI modified films.

increased the disorder of the perovskite bulk. Actually, based on the Scherrer equation, the grain size was inversely proportional to the value of the FWHM. Thus the results of XRD corresponded well with the size distribution from SEM images.

The presence of the passivation induced by PPEAI and its chemical bonding to the perovskite was further confirmed by Fourier transform infrared (FTIR) measurements (shown in Fig. S5†). As a comparison, we also measured the FTIR spectra of pure PPEAI. It can be seen that for the stretching vibration absorption of the carbon double bond (C=C) in the benzene rings, the spectral feature in free PPEAI was at 1476 cm^{-1}, while it shifted to a higher wavenumber at 1465 cm^{-1} when observed in the PPEAI-modified perovskite film. This red shift phenomenon was indicative of the combination between the PPEAI molecules and other chemical groups. Thus we think that the Fourier transform infrared (FTIR) measurement could further confirm the chemical bonding of PPEAI to the perovskite framework.

To study the optical characteristics, absorption spectra and PL of the different films were measured. Actually, there was almost no difference among the control and PPEAI-modified films from the optical images, as shown in Fig. S6.† With the PPEAI modified film, the absorption intensity of band edges of the absorption spectra was almost invariant (shown in Fig. 2f). The normalized PL spectra of the perovskite films are shown in Fig. 2g; with the

increase of the concentration of PPEAI, the PL peak of the corresponding films shifted slightly. When compared with the pristine perovskite film, the PL spectra of PPEAI modified films (1 mg mL^{-1} PPEAI, 2 mg mL^{-1} PPEAI and 5 mg mL^{-1} PPEAI) indicated blue shifting of 3 nm, 7 nm, and 11 nm, respectively. Such blue shifting could be attributed to a decrease of spontaneous nonradiative recombination from the trap states.[33,34]

In order to investigate the change in work function before and after post-treatment with PPEAI, ultraviolet photoelectron spectroscopy (UPS) measurements were utilized, as shown in Fig. S7 in the ESI.† Here the cut-off binding energies ($E_{cut-off}$) of different films (as-prepared, 1 mg mL^{-1} PPEAI, 2 mg mL^{-1} PPEAI and 5 mg mL^{-1} PPEAI) were 16.94, 16.89, 16.87 and 16.83 eV, respectively. Work functions (W_F) of different films (as-prepared, 1 mg mL^{-1} PPEAI, 2 mg mL^{-1} PPEAI and 5 mg mL^{-1} PPEAI) were calculated to be 4.28, 4.33, 4.35 and 4.39 eV according to the formula of $W_F = 21.22 - E_{cut-off}$, respectively. It can be seen that the work function of films modified with PPEAI was slightly downshifted as compared to that of the control film. Considering that the LUMO of C$_{60}$ was 4.5 eV, the treatment of PPEAI was beneficial for reducing the potential difference between perovskite and C$_{60}$, promoting the charge extraction to some extent.

Based on the analysis of the morphology, absorption and XRD, we speculated that the introduced PPEAI mainly

passivated the surface and GBs of the perovskite film, while the active bulk still maintained the quasi-3D structure.

J–V curves

To evaluate the passivation effect of PPEAI on the photovoltaic performance systematically, a series of concentrations of PPEAI (1 mg mL^{-1}, 2 mg mL^{-1}, and 5 mg mL^{-1}) was used to prepare the perovskite films, and a typical inverted planar hetero-junction structure (ITO/PTAA/LiF/perovskite/C60/BCP/Ag) was employed as the solar cell device (schematic diagram is shown in Fig. 3a and b). The current density–voltage (J–V) curves of the various devices are shown in Fig. 3c, and the statistical analysis of device performance parameters of 30 devices for different structures is presented in Fig. S8 and Table S1.† Here the typical device with the control perovskite film exhibited a J_{sc} of 21.53 mA cm^{-2}, a V_{oc} of 1.068 V, a fill factor of 0.742 and a power conversion efficiency (PCE) of 17.04%. With the optimal PPEAI concentration (2 mg mL^{-1}), the representative performance of the device showed a V_{oc} of 1.12 V, a FF of 0.785, and a J_{sc} of 22.89 mA cm^{-2}, and a PCE of 20.12% with better reproducibility compared to that of the reference. It can be noted that while

processing the PPEAI modification, the device performance shows an increase-to-decrease tendency, with comparatively better performance of 1 mg mL^{-1} and 2 mg mL^{-1} and reduced efficiency of 5 mg mL^{-1}. Considering the low activation energy from the 3D to 2D structure, high concentration PPEAI may not only passivate the surface traps but also substitute some FA$^+$/MA$^+$ cations in the original 3D perovskite film.[35] Thus the reduced performance can be attributed to the formation of an excessively insulating hydrophobic passivation layer cover on the 3D framework.

Hysteresis is one serious issue for PSCs, and originates mainly from the halide ion migration associated with phase segregation.[36] As shown in Fig. 3d, the best device with the control film showed a PCE of 17.98% (17.05%), a J_{sc} of 21.71 mA cm^{-2} (21.67 mA cm^{-2}), a V_{oc} of 1.078 V (1.075 V) and a FF of 0.769 (0.732) for reverse and forward scanning. When referring to the best device with the PPEAI-modified film (2 mg mL^{-1}), improved performance was obtained with a J_{sc}, V_{oc}, FF, and PCE of 23.02 mA cm^{-2} (22.99 mA cm^{-2}), 1.126 V (1.124 V), 0.809 (0.793), and 21.01% (20.49%) for reverse and forward scanning. Here the PPEAI-modified devices showed a lower hysteresis
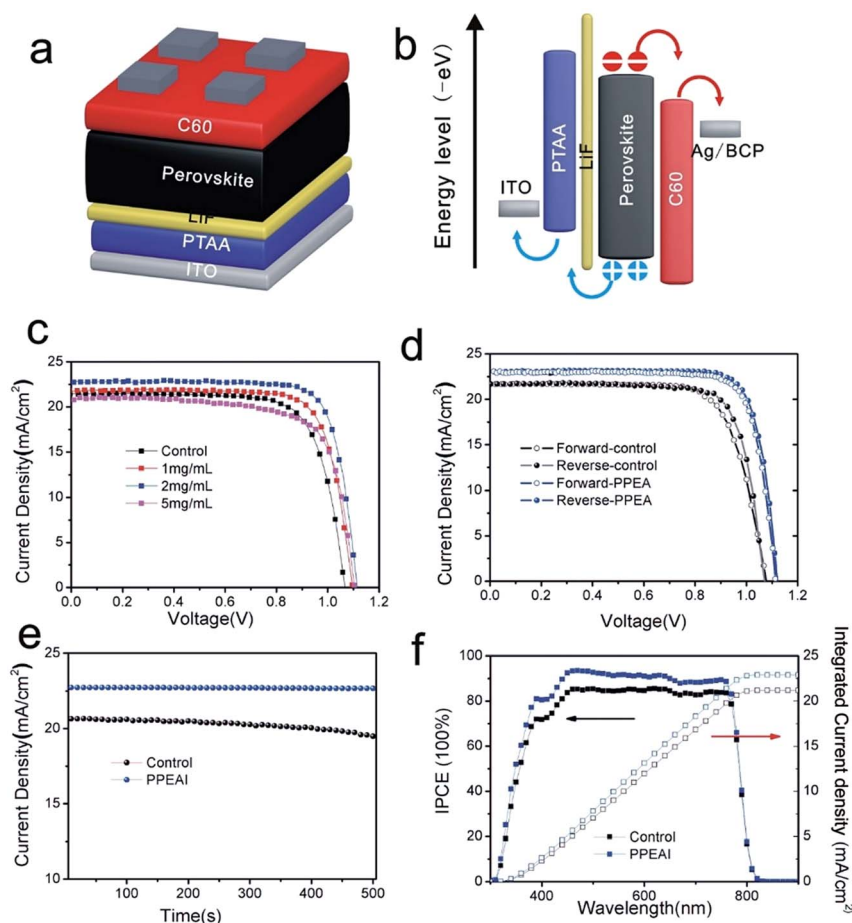

Fig. 3 (a) Schematic structure and (b) energy level diagram of P–I–N planar heterojunction perovskite solar cells (PSCs); (c) representative J–V curves of PSCs fabricated using control and PPEAI modified films; (d) J–V curves of champion PSCs with control and optimal PPEAI modified films under reverse and forward scanning; (e) stabilized current density output of the champion PSCs with control and optimal PPEAI modified films under P_{max} (V_{bis} = 0.917 V and V_{bis} = 0.875 V); (f) IPCE spectra of PSCs based on control and 2 mg mL^{-1} PPEAI films.

than the control devices, which may be related to the suppressed ion migration by the formation of a low dimensional capping layer on the surface and GBs of the perovskite film. Fig. 3e shows the comparison of stabilized current density of the reference and PPEAI-treated (2 mg mL^{-1}) devices with a test for 500 s, and the modified device shows a more stable output. The incident photon-to-current conversion efficiency (IPCE) spectra of the reference and PPEAI-modified (2 mg mL^{-1}) devices are shown in Fig. 3f. Here a stronger external quantum efficiency of the modified device can be observed compared to that of the reference one. The integration of the IPCE spectrum with the AM 1.5 solar emission spectrum produced a photocurrent that is consistent with the J_{sc} derived from the J–V curve.

Mechanism of recombination and transport dynamics

To understand the improvement of both V_{oc} and J_{sc} in the performance of the PPEAI modified devices, time-resolved photoluminescence (TRPL) measurements and electrochemical impedance spectroscopy (EIS) measurements were carried out to investigate the charge dynamics in the perovskite film and devices. Here the TRPL curves were fitted with a bi-exponential

decay function of time (t): $I(t) = I_0 + A_1 \exp(-t/\tau_1) + A_2 \exp(-t/\tau_2)$, where τ_1 and τ_2 represent the fast and slow decay time constant, and the lifetime $\tau_{average} = (A_1\tau_1^2 + A_2\tau_2^2)/(A_1\tau_1 + A_2\tau_2)$. By analyzing the data in Fig. 4a, the PPEAI modified perovskite film exhibited a longer lifetime (575 ns) compared to the as-prepared film (421 ns), indicating the reduced non-radiative recombination of the modified perovskite film *via* PPEAI post-treatment.[37,38]

In order to study the bulk and interfacial carrier dynamics in the devices, electrochemical impedance spectroscopy (EIS) measurements were carried out for the control and the PPEAI modified devices. A simplified circuit model is given in the inset. The high-frequency and middle-frequency arcs are associated with the bulk (R_{bulk}) and surface (R_{sur}) recombination resistances of the device.[39,40] It can be seen that for the PPEAI modified devices, the arc in the middle-frequency regime was obviously larger when compared to that of the control device, suggesting the increased recombination resistance for the PPEAI modified sample.

To gain insight into the trap healing effect of PPEAI, we fabricated perovskite film-based electron/hole-only devices. The corresponding single-carrier structures were as follows: ITO/TiO$_2$/perovskite/C60/Ag (electrons only) and ITO/PEDOT/
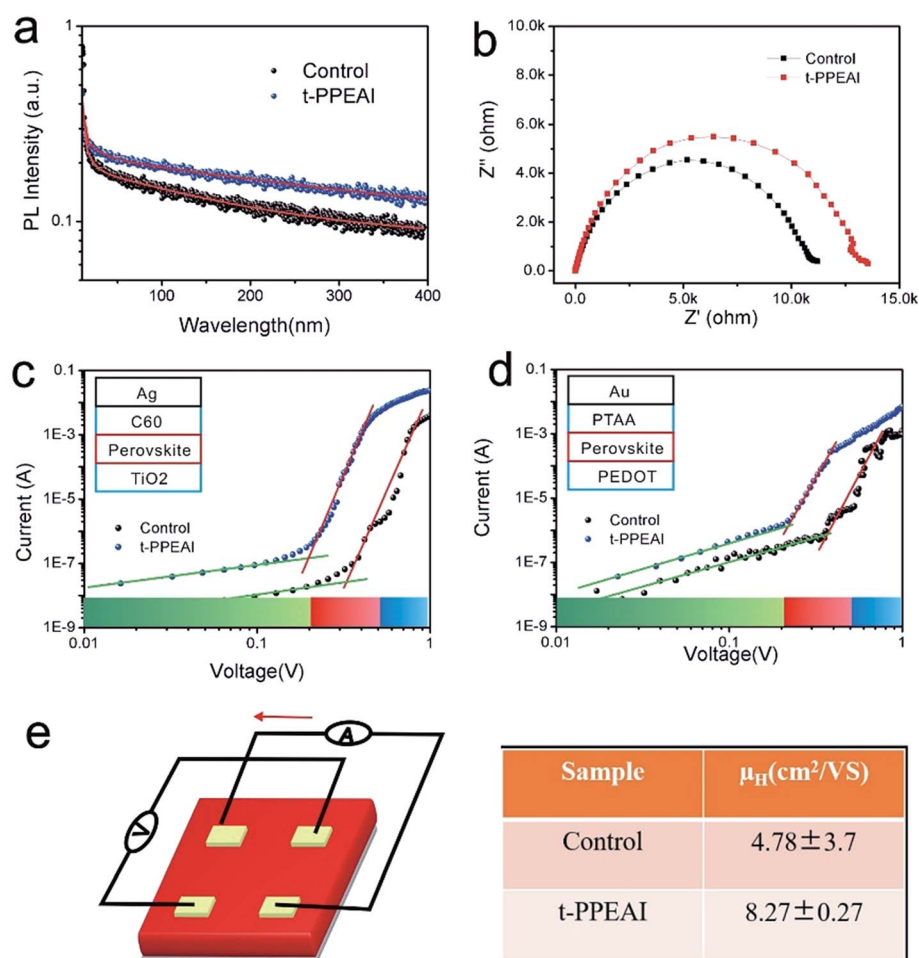

Fig. 4 (a) PL lifetime decay of control and optimal PPEAI modified perovskite films; (b) EIS measurements of PSCs based on control and optimal PPEAI modified perovskite films; current density–voltage (J–V) characteristics of (c) electron-only and (d) hole-only devices with OA-QDs and control and optimal PPEAI modified perovskite films; (e) Hall effect schematic diagram and corresponding measured results of control and optimal PPEAI modified perovskite films.

Sample	μ_H (cm²/VS)
Control	4.78±3.7
t-PPEAI	8.27±0.27

This journal is © The Royal Society of Chemistry 2019

J. Mater. Chem. A, 2019, **7**, 16533–16540 | **16537**

perovskite/PTAA/Au (holes only). The logarithm of the *I–V* curve in the dark is shown in Fig. 4c and d, and can be divided into three regions: linear ohmic response (slope = 1); nonlinear trap-filled response (slope > 2); space charge limited current (SCLC) response (slope = 2). In region 2, the bias-voltage at the inflection point was known as the trap-filled limit voltage (V_{TFL}).[41] The voltage at which all the traps are filled is determined from the trap density:[42]

$$N_{trap} = eL^2/V_{TFL}(2\varepsilon\varepsilon_0),$$

where L is the thickness of the perovskite film, and ε is the permittivity of the perovskite materials. The hole-trap densities of control and PPEAI modified films were calculated to be 5.95×10^{15} and 2.76×10^{15} cm^3, respectively. The electron trap densities were 6.21×10^{15} and 3.02×10^{15} cm^3, respectively. It can be seen that in the PPEAI modified structures, both the electron defect-state density and hole defect-state density decrease evidently, indicating the effective surface/GB trap state passivation of PPEAI. The decrease of trap states results in decreased recombination, contributing to the increased V_{oc} and efficiency of the solar cell devices.

In general, π-conjugated molecules or polymers can show a high charge transporting character owing to the delocalization of the molecular electronic orbitals.[30] Actually, by investigating the current densities of single carrier devices in Fig. 4c and d, a larger current density of the PPEAI modified sample can be observed compared to that of the control sample at the same voltage, revealing the improved charge transport characteristics of the PPEAI modified film. We also experimentally studied the sheet Hall effect of the control film and PPEAI modified film to further confirm whether conjugated ligands were favorable for carrier transport. The schematic illustration of the sheet Hall effect measurement is shown in Fig. 4e. Results show that the carrier mobilities (μH) of the control film and PPEAI modified (2

mg mL^{-1}) film were 4.78 ± 3.7 cm^2 V^{-1} s^{-1} and 8.27 ± 0.27 cm^2 V^{-1} s^{-1}, respectively. Based on the analysis of the single carrier and Hall characteristics, it could be substantially deciphered that the conjugated PPEAI could dramatically improve the charge transporting ability of the perovskite bulk.

Actually, due to the under-coordinated ions at perovskite crystal surfaces and at the grain boundaries (GBs), poor charge exchange/transport occurred between individual crystals. Here the introduction of PPEAI as the "conductive channel" between neighboring perovskite crystal fragments promoted the charge transporting efficiency of the perovskite bulk (shown in Fig. 5a). Density functional theory (DFT) calculations were also carried out to investigate the influence of the conjugated geometry configuration on the molecular structure and electron distribution. As shown in Fig. 5b–d, it can be seen that both the benzene ring part and alkyl chain part contributed to the HOMO and LUMO, which demonstrated the excellent conductivity of this aniline molecule.

Stability of the PSCs effected by PPEAI

In addition to the optoelectronic performance, the moisture/operating stability of the device effected by the PPEAI was also investigated. Benefitting from the long-chain structure and hydrophobic benzene ring, a large water contact angle ($\theta = 78°$) of the PPEAI modified film was observed compared to that of the control film ($\theta = 38°$) (shown in Fig. S9,†). In an ambient atmosphere at room temperature and a relative humidity of 40%, the control devices exhibited a very fast degradation tendency, whereas the PPEAI modified devices still retained 92% of the original PCEs over 1000 h. This result conclusively confirmed that the introduction of PPEAI could effectively improve the moisture stability of PSCs.

As for the operating stability (shown in Fig. S10b†), the control device completely degraded within 100 h. Interestingly, the PPEAI modified device maintained 85% of the original PCE
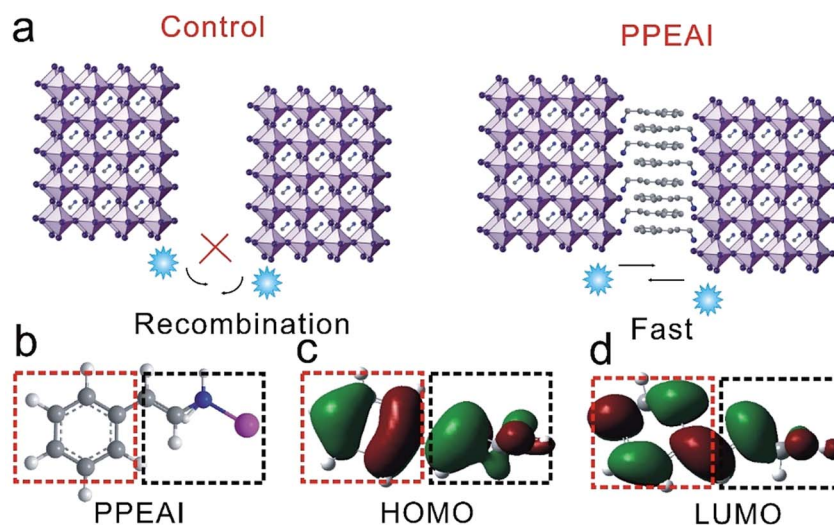

Fig. 5 (a) Schematic diagram of the conductive ability of PPEAI; (b) the structure of PPEAI; the HOMO (c) and LUMO (d) of the molecule. Here the red and black dashed lines represent the benzene ring and alkyl chain. The calculations were performed using the Gaussian 09 program at the B3LYP/631 G(d,p) level in a vacuum.

16538 | *J. Mater. Chem. A*, 2019, **7**, 16533–16540

This journal is © The Royal Society of Chemistry 2019

under 1 sun continuous illumination after 300 h. This result reveals that the PPEAI treatment could also improve the stability of PSCs under light-soaking. Fig. S10c and d† show the corresponding XRD results of the aged devices. The much slower reduction of the perovskite (110) plane peak and the slower appearance of the PbI$_2$ peak in the PPEAI modified PSCs further demonstrate the better moisture resistance capability enabled by the post-device modification. Actually, the low dimensional perovskites on the surface/GBs of the 3D framework induced by PPEAI could play the role of an encapsulation cover due to their hydrophobic terminal groups, which prevent moisture corrosion and ion migration effectively.

Conclusions

To sum up, a typical amine molecule, PPEAI, was employed as a functional passivator to simultaneously improve the stability and efficiency of the PSCs. By regulating the crystallization process of the perovskite active layer, PPEAI could effectively passivate the traps on the surface/GBs of the film, thus reducing the interfacial/bulk non-radiative recombination. Moreover, benefitting from the unique π-conjugation and delocalization property of PPEAI, improved carrier-transport was observed in the modified film, which cannot be achieved by conventional long-chain ligands. With an optimized amount of PPEAI, the best device shows a superior PCE of 21.01% and excellent stability. This work proposes a facile and efficient strategy to enhance the optoelectronic performance of PSCs and could inspire more studies to further improve both the performance and stability of PSCs.

Experimental details

Fabrication of the perovskite film

The triple cation perovskite (FA$_{0.85}$MA$_{0.15}$)$_{0.95}$Cs$_{0.05}$Pb(I$_{0.85}$Br$_{0.15}$)$_3$ layer was deposited by a one-step method. FAI and MABr were purchased from Dyesol. PbI$_2$ and PbBr$_2$ were from TCI, and CsI was from Sigma Aldrich. A mixed solution of FAI (1 M), PbI$_2$ (1.1 M), MABr (0.2 M) and PbBr$_2$ (0.2 M) was dissolved in dimethylformamide (DMF) and dimethyl sulfoxide (DMSO) (4 : 1, v/v) with an excess amount of PbI$_2$. A 1.5 M solution of CsI was added into the mixed solution forming the composition required. The triple cation solution was spin-coated on the substrate with a two step program at 2000 rpm and 6000 rpm for 10 s and 30 s, respectively. During the second step, 250 μL chlorobenzene was dropped on the spinning substrate after 20 s. To prepare the antisolvent with PPEAI, 1, 2 and 5 mg PPEAI were respectively dissolved in 1 mL chlorobenzene (CB) and stirred for 2 h to yield a completely dissolved solution. Then, the film was quickly annealed at 120 °C for 10 min.

Fabrication of PSCs

Firstly, indium tin oxide (ITO) patterned glass substrates with a sheet resistance of about 15 Ω square^{-1} were cleaned with deionized water and organic solvents, and then exposed to UV-ozone ambience for 5 min. Secondly, PTAA solution (2 mg mL^{-1}

in chlorobenzene) was spin-coated at 5000 rpm for 30 s on cleaned ITO glass and then annealed at 120 °C for 20 min. After this, the ITO/PTAA substrates were transferred into a nitrogen-filled glove box, and the (FA$_{0.85}$MA$_{0.15}$)$_{0.95}$Cs$_{0.05}$Pb(I$_{0.85}$Br$_{0.15}$)$_3$ perovskite films were fabricated following the process above. Eventually, the devices were completed by consecutively vacuum depositing C$_{60}$ (30 nm), BCP (8 nm) and a Ag cathode (120 nm) under 10^{-3} mbar.

Characterization

A field emission scanning electron microscope (SEM) (Quanta 250, FEI, USA) was used to investigate the morphology and crystallinity. The crystalline structure on the ITO substrate was obtained using an X-ray diffractometer (Bruker D8 ADVANCE) with Cu Kα radiation. The absorption spectra were obtained using a UV-vis spectrophotometer (HITACHI U-3010, Japan). The time-resolved PL spectra were recorded by 100 ps time resolution using a time-correlated single photon counting (TCSPC) system (FLS920 spectrometer) (excited by picosecond pulsed LEDs, pulse duration: <850 ps, repetition rate: 10 MHz). The FTIR spectra were recorded with a Bruker V70 spectrophotometer. The UPS characterization was carried out by X-ray photoelectron spectroscopy (ESCALAB Xi+, Thermo Fisher Scientific). The photovoltaic performance was estimated with an AAA solar simulator (XES-301S, SAN-EI), under AM 1.5G irradiation with an intensity of 100 mW cm^{-2}. The photocurrent–voltage (J–V) curve was measured using a Keithley (2602 Series Sourcemeter), and the scanning was performed with a 0.2 V s^{-1} step. Incident photon-to-current conversion efficiency (IPCE) spectra were collected in AC mode using a solar cell quantum efficiency measurement system (SolarCellScan 100, Zolix instruments. Co. Ltd). The area of each device, calibrated with a shadow mask, was 9.00 mm^2. Electrochemical impedance spectra (EIS) of the cells were obtained using a CHI-660E over the frequency range of 0.1 Hz to 100 KHz under illumination (100 mW cm^{-2}).

Conflicts of interest

There are no conflicts to declare.

Acknowledgements

Notes and references

1 A. Kojima, K. Teshima, Y. Shirai and T. Miyasaka, *J. Am. Chem. Soc.*, 2009, **131**, 6050.

2 https://www.nrel.gov/pv/assets/pdfs/pv-efficiency-chart.201901.

3 N. J. Jeon, H. Na, E. H. Jung, T. Y. Yang, Y. G. Lee, G. Kim, H. W. Shin, S. I. Seok, J. Lee and J. Seo, *Nat. Energy*, 2018, **3**, 682.

4 J. Xi, K. Xi, A. Sadhanala, K. H. L. Zhang, G. R. Li, H. Dong, T. Lei, F. Yuan, C. X. Ran, B. Jiao, P. R. Coxon, C. J. Harris, X. Hou, R. V. Kumar and Z. X. Wu, *Nano Energy*, 2019, **56**, 741–750.

5 W. Y. Gao, C. X. Ran, J. Xi, B. Jiao, W. W. Zhang, M. C. Wu, X. Hou and Z. X. Wu, *ChemPhysChem*, 2018, **19**, 1696–1700.

6 S. D. Stranks, G. E. Eperon, G. Grancini, C. Menelaou, M. J. P. Alcocer, T. Leijtens, L. M. Herz, A. Petrozza and H. J. Snaith, *Science*, 2013, **342**, 341–344.

7 Y. X. Zhao and K. Zhu, *Chem. Soc. Rev.*, 2016, **45**, 655–689.

8 D. Y. Luo, W. Q. Yang, Z. P. Wang, A. Sadhanala, Q. Hu, R. Su, R. Shivanna, G. F. Trindade, J. F. Watts, Z. J. Xu, T. H. Liu, K. Chen, F. J. Ye, P. Wu, L. C. Zhao, J. Wu, Y. G. Tu, Y. F. Zhang, X. Y. Yang, W. Zhang, R. H. Friend, Q. H. Gong, H. J. Snaith and R. Zhu, *Science*, 2018, **360**, 1442–1446.

9 H. S. Kim, C. R. Lee, J. H. Im, K. B. Lee, T. Moehl, A. Marchioro, S. J. Moon, R. Humphry-Baker, J. H. Yum, J. E. Moser, M. Gratzel and N. G. Park, *Sci. Rep.*, 2012, **2**, 591.

10 J. W. Lee, D. J. Seol, A. N. Cho and N. G. Park, *Adv. Mater.*, 2014, **26**, 4991–4998.

11 M. Saliba, T. Matsui, J. Y. Seo, K. Domanski, J. P. Correa-Baena, M. K. Nazeeruddin, S. M. Zakeeruddin, W. Tress, A. Abate, A. Hagfeldt and M. Gratzel, *Energy Environ. Sci.*, 2016, **9**, 1989–1997.

12 W. S. Yang, B. W. Park, E. H. Jung, N. J. Jeon, Y. C. Kim, D. U. Lee, S. S. Shin, J. Seo, E. K. Kim, J. H. Noh and S. I. Seok, *Science*, 2017, **356**, 1376.

13 H. Dong, J. Xi, L. J. Zuo, J. R. Li, Y. G. Yang, D. D. Wang, Y. Yu, L. Ma, C. X. Ran, W. Y. Gao, B. Jiao, J. Xu, T. Lei, F. J. Wei, F. Yuan, L. Zhang, Y. F. Shi, X. Hou and Z. X. Wu, *Adv. Funct. Mater.*, 2019, 1808119.

14 X. T. Meng, X. Cui, M. Rager, S. G. Zhang, Z. W. Wang, J. Yu, Y. W. Harn, Z. T. Kang, B. K. Wagner, Y. Liu, C. Yu, J. S. Qiu and Z. Q. Lin, *Nano Energy*, 2018, **52**, 123–133.

15 M. He, B. Li, X. Cui, B. B. Jiang, Y. J. He, Y. H. Chen, D. O'Neil, P. Szymanski, M. A. El-Sayed, J. S. Huang and Z. Q. Lin, *Nat. Commun.*, 2017, **8**, 16045.

16 M. D. Ye, C. F. He, J. Iocozzia, X. Q. Liu, X. Cui, X. T. Meng, M. Rager, X. D. Hong, X. Y. Liu and Z. Q. Lin, *J. Phys. D: Appl. Phys.*, 2017, **50**, 112829.

17 M. He, X. C. Pang, X. Q. Liu, B. B. Jiang, Y. J. He, H. Snaith and Z. Q. Lin, *Angew. Chem., Int. Ed.*, 2016, **55**, 4280–4284.

18 M. He, D. J. Zheng, M. Y. Wang, C. J. Lin and Z. Q. Lin, *J. Mater. Chem. A*, 2014, **2**, 5994–6003.

19 L. Zhang, F. Yuan, H. Dong, B. Jiao, W. W. Zhang, X. Hou, S. F. Wang, Q. H. Gong and Z. X. Wu, *ACS Appl. Mater. Interfaces*, 2018, **10**, 40661–40671.

20 H. Dong, T. Lei, F. Yuan, J. Xu, Y. Niu, B. Jiao, Z. X. Zhang, D. W. Ding, X. Hou and Z. X. Wu, *Org. Electron.*, 2018, **60**, 1–8.

21 T. Lei, H. Dong, J. Xi, Y. Niu, J. Xu, F. Yuan, B. Jiao, W. W. Zhang, X. Hou and Z. X. Wu, *Chem. Commun.*, 2018, **54**, 6177–6180.

22 F. Yuan, J. Xi, H. Dong, K. Xi, W. W. Zhang, C. X. Ran, B. Jiao, X. Hou, A. K. Y. Jen and Z. X. Wu, *Phys. Status Solidi RRL*, 2018, **12**, 1800090.

23 Y. F. Shi, W. Wu, H. Dong, G. R. Li, K. Xi, G. Divitini, C. X. Ran, F. Yuan, M. Zhang, B. Jiao, X. Hou and Z. X. Wu, *Adv. Mater.*, 2018, **30**, 1800251.

24 C. X. Ran, J. Xi, W. Y. Gao, F. Yuan, T. Lei, B. Jiao, X. Hou and Z. X. Wu, *ACS Energy Lett.*, 2018, **3**, 713.

25 P. Chen, Y. Bai, S. C. Wang, M. Q. Lyu, J. H. Yun and L. Z. Wang, *Adv. Funct. Mater.*, 2018, **28**, 1706923.

26 F. Wang, W. Geng, Y. Zhou, H. H. Fang, C. J. Tong, M. A. Loi, L. M. Liu and N. Zhao, *Adv. Mater.*, 2016, **28**, 9986–9992.

27 T. Ye, A. Bruno, G. F. Han, T. M. Koh, J. Li, N. F. Jamaludin, C. Soci, S. G. Mhaisalkar and W. L. Leong, *Adv. Funct. Mater.*, 2018, **28**, 1801654.

28 Y. Bai, S. Xiao, C. Hu, T. Zhang, X. Y. Meng, H. Lin, Y. L. Yang and S. H. Yang, *Adv. Energy Mater.*, 2017, **7**, 1701038.

29 J. Z. Chen, J. Y. Seo and N. G. Park, *Adv. Energy Mater.*, 2018, **8**, 1702714.

30 J. F. Dai, J. Xi, L. Li, J. F. Zhao, Y. F. Shi, W. W. Zhang, C. X. Ran, B. Jiao, X. Hou, X. H. Duan and Z. X. Wu, *Angew. Chem., Int. Ed.*, 2018, **57**, 5754–5758.

31 H. Zhang, X. G. Ren, X. W. Chen, J. Mao, J. Q. Cheng, Y. Zhao, Y. H. Liu, J. Milic, W. J. Yin, M. Gratzel and W. C. H. Choy, *Energy Environ. Sci.*, 2018, **11**, 2253–2262.

32 K. M. M. Salim, T. M. Koh, D. Bahulayan, P. C. Harikesh, N. F. Jamaludin, B. Febriansyah, A. Bruno, S. Mhaisalkar and N. Mathews, *ACS Energy Lett.*, 2018, **3**, 1068–1076.

33 Y. Z. Lin, L. Shen, J. Dai, Y. H. Deng, Y. Wu, Y. Bai, X. P. Zheng, J. Y. Wang, Y. J. Fang, H. T. Wei, W. Ma, X. C. Zeng, X. W. Zhan and J. S. Huang, *Adv. Mater.*, 2017, **29**, 1604545.

34 F. Zhang, W. D. Shi, J. S. Luo, N. Pellet, C. Y. Yi, X. Li, X. M. Zhao, T. J. S. Dennis, X. G. Li, S. R. Wang, Y. Xiao, S. M. Zakeeruddin, D. Q. Bi and M. Gratzel, *Adv. Mater.*, 2017, **29**, 1606806.

35 T. Zhao, C. C. Chueh, Q. Chen, A. Rajagopal and A. K. Y. Jen, *ACS Energy Lett.*, 2016, **1**, 757–763.

36 D. J. Slotcavage, H. I. Karunadasa and M. D. McGehee, *ACS Energy Lett.*, 2016, **1**, 1199–1205.

37 W. Z. Li, W. Zhang, S. Van Reenen, R. J. Sutton, J. D. Fan, A. A. Haghighirad, M. B. Johnston, L. D. Wang and H. J. Snaith, *Energy Environ. Sci.*, 2016, **9**, 490–498.

38 M. Zhang, H. Yu, M. Q. Lyu, Q. Wang, J. H. Yun and L. Z. Wang, *Chem. Commun.*, 2014, **50**, 11727–11730.

39 F. Fabregat-Santiago, G. Garcia-Belmonte, I. Mora-Sero and J. Bisquert, *Phys. Chem. Chem. Phys.*, 2011, **13**, 9083–9118.

40 J. Bisquert, *J. Phys. Chem. B*, 2002, **106**, 325–333.

41 J. J. Peng, Y. N. Chen, K. B. Zheng, T. Pullerits and Z. Q. Liang, *Chem. Soc. Rev.*, 2017, **46**, 5714–5729.

42 J. F. Yuan, L. X. Zhang, C. H. Bi, M. R. Wang and J. J. Tian, *Sol. RRL*, 2018, **2**, 1800188.

16540 | *J. Mater. Chem. A*, 2019, **7**, 16533–16540

This journal is © The Royal Society of Chemistry 2019